ChemComm

COMMUNICATION

View Article Online
View Journal | View Issue

Cite this: *Chem. Commun.*, 2025, **61**, 5019

Received 28th November 2024,
Accepted 14th February 2025

DOI: 10.1039/d4cc06320a

rsc.li/chemcomm

Structural insights of mechanochemically amorphised MIL-125-NH_2†

Emily V. Shaw, [a] Celia Castillo-Blas, *[a] Timothy Lambden,[a] Beatriz de Santos, [b] Bethan Turner, [c] Giulio I. Lampronti, [a] Joonatan E. M. Laulainen,[a] Georgina P. Robertson,[ad] Ashleigh M. Chester, [a] Chumei Ye,[ae] Shaoliang Guan,[ae] Joshua K. G. Karlsson,[a] Valentina Martinez, [f] Ivana Brekalo, [f] Bahar Karadeniz,[f] Silvia Cabrera, [gh] Lauren N. McHugh, [c] Krunoslav Užarević, [f] Jose Alemán, [bh] Alberto Fraile, [bh] Rachel C. Evans, [a] Paul A. Midgley,[a] David A. Keen, [i] Xavier Moya[a] and Thomas D. Bennett*[j]

In this work, we investigated the response of the metal–organic framework MIL-125-NH_2 to ball-milling. Both localised and bulk analyses revealed prolongued ball-milling results in a complete loss of long-range structural order. Investigation of this disorder revealed partial retention of the local bonding of the secondary building unit, suggesting structure collapse progressed primarily through metal–linker bond breakage. We explored the photocatalytic performance of the materials, and examined the materials' band gap using UV-Vis reflectance spectroscopy.

Amorphous metal–organic frameworks (*a*MOFs) have gained increased attention thanks to their facile synthesis and promising physical and chemical properties.[1] These *a*MOFs preserve the interconnected nature of the parent crystalline material, whilst lacking any correlated long-range order.[1,2] Formation of *a*MOFs can be achieved through several methodologies, including direct synthesis, thermal treatment or application of mechanical shear stress, frequently resulting in a non-reversible transition to a disordered structure.[3]

The high concentration of intrinsic defects in *a*MOFs often enhances the functionalities, acting as the active sites for both catalysis and gas sorption applications.[4,5] However, amorphisation typically reduces their porosity compared to the crystalline parent materials. Despite this, *a*MOFs have been utilised as slow drug release systems, also displaying improved gas selectivity and separation, compared to crystalline equivelents.[6] Therefore, understanding the structural effects of amorphisation has become crucial for predicting the properties of these amorphous materials for their potential applications.

Ball-milling has been shown to reduce crystallite size and introduce structural defects, which, at critical concentrations, leads to structural distortion and eventual collapse into a highly disordered, amorphous state.[7,8] Several MOFs, *e.g.*, Zn-ZIF-8, Al-ndc and Zn-MOF-74, retain their extended X-ray absorption fine structure (EXAFS) profiles upon mechanical amorphisation, indicating a retention of the short-range order (SRO) and secondary building unit (SBU).[8] In contrast, ball-milled UiO-66 exhibits distortion of its $Zr_6O_4(OH)_4$ SBU during amorphisation,[9] which progresses *via* the breakage of metal–linker (M–L) bonds, as suggested by X-ray pair distribution (XPDF) anaylsis.[10]

Here we present a structural study of mechanically amorphised MIL-125-NH_2 using powder X-ray diffraction (PXRD), scanning electron diffraction (SED) and X-ray pair distribution function (XPDF) analysis. The optical properties of this photoactive material were evaluated using ultraviolet-visible (UV-Vis) spectroscopy. MIL-125-NH_2, $[Ti_8O_8OH_4(H_2N\text{-}bdc)_6]$ (bdc = benzene-1,4-dicarboxylic acid, $C_8H_7NO_4$) is a titanium-MOF isostructural to MIL-125 (Fig. 1a), consisting of a porous three-dimensional quasi cubic tetragonal structure with **fcu** topology possessing tetrahedral and octahedral cages.[11] The SBU is defined as an $Ti_8O_8(OH)_4$ octameric ring of eight titanium oxo-clusters with corner and edge-sharing TiO_6 octahedral units.

MIL-125-NH_2 was prepared following a modified reported synthetic procedure (see ESI,† methods).[13] Phase purity was confirmed by PXRD and Pawley refinement (Fig. S2 and Table S1, ESI†). Upon ball-milling of crystalline MIL-125-NH_2, rapid

[a] *Department of Materials Science & Metallurgy, University of Cambridge, 27 Charles Babbage Road, Cambridge, UK. E-mail: cc2078@cam.ac.uk*
[b] *Organic Chemistry Department, Science Faculty, Universidad Autónoma de Madrid, C/ Francisco Tomás y Valiente, 7, 28049 Madrid, Spain*
[c] *Department of Chemistry, University of Liverpool, Crown Street, Liverpool L69 7ZD, UK*
[d] *Diamond Light Source Ltd., Diamond House, Harwell Campus, Didcot, Oxfordshire, UK*
[e] *Maxwell Centre, Cavendish Laboratory, University of Cambridge, J.J. Thomson Avenue, Cambridge, CB3 0HE, UK*
[f] *Division of Physical Chemistry, Ruđer Bošković Institute, Zagreb, Croatia*
[g] *Inorganic Chemistry Department, Science Faculty, Universidad Autónoma de Madrid, C/ Francisco Tomás y Valiente, 7, 28049 Madrid, Spain*
[h] *Institute for Advanced Research in Chemical Science (IAdChem), Universidad Autónoma de Madrid, C/ Francisco Tomás y Valiente, 7, 28049 Madrid, Spain*
[i] *ISIS Facility, Rutherford Appleton Laboratory, Harwell Campus, Didcot, Oxfordshire OX11 0QX, UK*
[j] *School of Physical and Chemical Sciences, University of Canterbury, Private Bag 4800, Christchurch 8140, New Zealand. E-mail: thomas.bennett@canterbury.ac.nz*

† Electronic supplementary information (ESI) available. See DOI: https://doi.org/10.1039/d4cc06320a

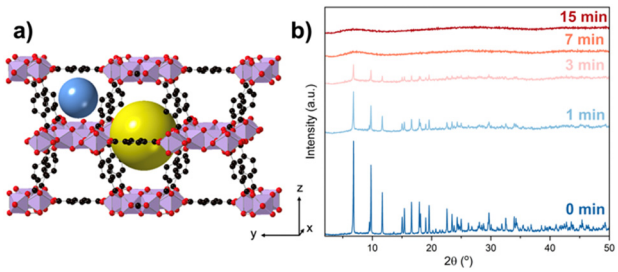

Fig. 1 (a) Structure of MIL-125, highlighting the pore cavities with two diameters (blue = 6.1 Å, yellow = 12.5 Å). Titanium polyhedra, oxygen and carbon are represented in purple, red and black, respectively. Hydrogen atoms are omitted for clarity. Structure calculated from a reported crystal structure.[12] (b) PXRD patterns of MIL-125-NH_2 as a function of duration of ball milling. Wavelength λ = 1.5418 Å.

loss of sharp Bragg intensities was observed in the PXRD (Fig. 1b and Fig. S3 and Table S2, ESI†). Amorphisation was complete after 15 minutes, with this sample referred to as a_mMIL-125-NH_2 (a_m = mechanochemically amorphised). *In situ* mechanochemical PXRD studies, performed at the P.02.1 beamline (DESY) (Fig. S4, ESI†), confirmed the timescale of this collapse. Sequential Rietveld refinements indicated that the unit cell parameters remained largely unchanged until ~6 minutes, at which point the crystallite size decreased to approximately the unit cell size, Fig. S5 (ESI†). Phase quantification suggested that amorphisation initially progressed through a reduction in crystallite size, with a delayed onset of amorphisation until ~8 minutes. Scanning electron microscopy (SEM) confirmed this decrease in crystallite size, and subsequent formation of aggregate clusters (Fig. S6, ESI†).

Scanning electron diffraction (Fig. 2), was utilised to probe the order at the nanoscale. This was operated at a low electron flux ($10e^- A^{-2} s^{-1}$) to reduce beam-induced damage commonly observed in MOFs and hybrid materials.[14] The crystalline Bragg spots observed in MIL-125-NH_2, Fig. 2d, are lost upon amorphisation of the sample, instead producing diffuse rings of scattering, Fig. 2e. This was quantified through the normalised variance as a function of reciprocal distance, Fig. 2f.

X-ray total scattering data were collected at P02.1 beamline of PETRA III (DESY) to investigate the SRO upon mechanical amorphisation. Bragg peak intensities decreased upon increased ball-milling time, consistent with SED, at a similar rate to PXRD (Fig. S7, ESI†). Signals >10 Å, indicating LRO, decreased with ball-milling time and were absent in a_mMIL-125-NH_2, (Fig. S8, ESI†). The XPDF of crystalline MIL-125-NH_2 showed long-range correlations, corresponding to order extending between SBUs, suggestive of an extended ordered structure (Fig. S8, ESI†).

Correlations of the SRO were calculated using an isolated SBU with PDFgui (Fig. S9, ESI†).[15] Comparing the SRO of the ball-milled *versus* crystalline samples revealed some retention of peak intensity and position, with deviations highlighted in the difference pattern (Fig. 3b). Identifying the structural origin of the changes upon amorphisation is challenging due to the complexity of the SBU structure. Partial PDFs were used (Fig. S10, ESI†) to investigate the origin of the contributions of each peak. Correlations involving hydrogen were excluded as they contributed minimally to the scattering. Key peak contributions are outlined in Table S3 (ESI†) and Fig. 3c. The loss of peak intensity for peaks at longer length scale confirmed the reduction of correlations extending across the linker (Fig. S12, ESI†). Changes in peak area are qualitatively illustrated in Fig. S12a (ESI†). SRO analysis revealed peak movement and broadening (Fig. S12b, ESI†), suggesting linker-SBU bond breakage (Fig. S9, ESI†), consistent with observations in UiO-66, MIL-100 and several ZIF species.[10,16,17]

Principal component analysis (PCA) of $D(r)$'s have previously been used to study structural distortions in *a*MOFs, such as Fe-BTC, as well as to investigate amorphisation by melting in TIF-4 material.[18] In this work, PCA of the PDF data at different ball-milling times (Fig. S13 and Tables S4, S5, ESI†) showed PC1 represents an average of the data sets, primarily containing information of the SRO. PC2 highlights the structural distortion upon amorphisation, shown by the equivalence to the

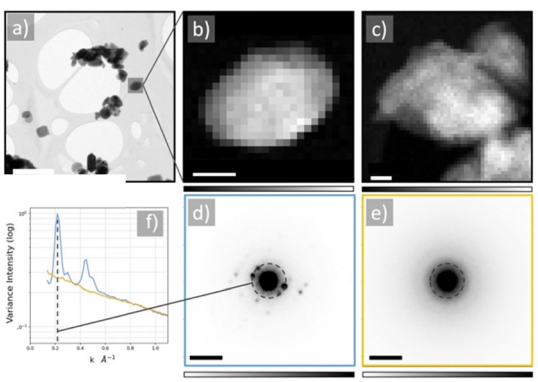

Fig. 2 SED of MIL-125-NH_2 (a) virtual bright-field image of crystalline MIL-125-NH_2, scale bar = 500 nm. Virtual high-angle annular dark-field (HAADF) images of (b) nanocrystal of crystalline MIL-125-NH_2 and (c) nanocrystal of a_mMIL-125-NH_2, scale bars = 50 nm. Summed area diffraction maps of these crystals are shown in (d) and (e), respectively, with scale bar = 2 nm^{-1}. (f) Normalised variance, measured azimuthally, of the diffraction maps in (d) (blue) and (e) (orange) with the central beam excluded. The observed peaks were assigned to (i) (002) (211), (ii) (112), (iii) (330) (iv) (004) crystal planes.

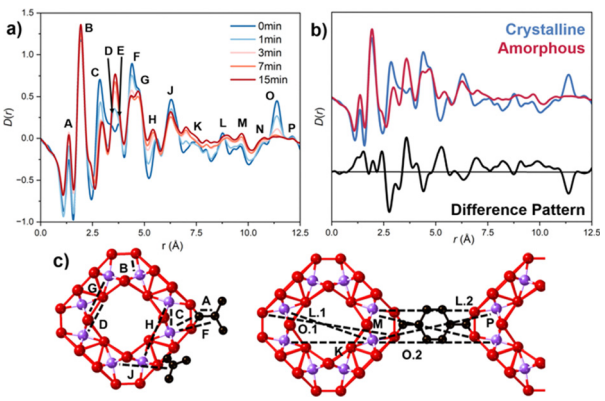

Fig. 3 (a) Pair distribution functions (PDF) of the ball-milled materials. Key shows the duration of milling in minutes. Labels correspond to some key correlations, marked in (c). (b) Comparison of SRO region of PDFs of crystalline and a_mMIL-125-NH_2. (c) SBU and MIL-125-NH_2 structure. Ti, O and C are denoted in purple, red and black, respectively.

difference pattern, Fig. S13b (ESI†). The significance of the structural distortion was illustrated by the high variance contribution, 8.83%. Peaks at high-*r* values indicated a reduction in LRO as ball-milling time increased, while low-*r* peaks suggested potential structural distortions. Strong peaks in PC2 located at peak F (4.35 Å) and between 5.68–6.46 Å (peaks H and J), are consistent with loss of Ti–C correlations, consistent with amorphisation progressing through metal–linker bond breakage, and the partial loss of linker. A prominent peak at 2.74 Å (peak C), showed rapid loss of intensity supporting this.

Several of the observed changes, however, cannot be explained for solely by M–L bond breakage, or the loss of long-range order. The coalescence of peaks D and E during amorphisation, which contributes to the observed increase in peak intensity, suggests a distortion within the SBU of the structure (Fig. S12b, ESI†). The observed increase in intensity could also be attributed to contributions from peak F, through compression of the Ti-SBU, or from peak C, through an increase of Ti–C bond length as a result of linker monocoordination. While initial decrease in intensity of peak H was attributed to the loss of Ti–C interactions, the shift to shorter distances is supportive of a lateral collapse of the SBU structure. The subsequent increase in peak intensity is likely as a result of both this, and the broadening of peak G. Beyond this point, it deconvolution of structural changes from the loss of LRO was not possible.

X-ray photoelectron spectroscopy was used to investigate this potential change further (Fig. S15, ESI†). The deconvolution of O 1s, N 1s, C 1s and Ti 2p signals were consistent with literature (Fig. S16 and S17, ESI†). The binding energies showed little variation in the binding environments between the crystalline and amorphous samples. The Ti–O contribution was reduced upon amorphisation, Table S6 (ESI†), consistent with the breakage of these SBU-based bonds. This might indicate the formation of alternative SBU structures rather than just distortions, and potential formation of TiO_2 nanodomains. The increased O–H signal upon amorphisation supports the idea of M–L bond breakage. Simulated PDFs for other Ti-based MOF containing different SBUs (*e.g.*, MOF-901 (Ti_6O_6), MIL-177 (Ti_6O_9), COK-69 (Ti_3O_6) or NTU-9) showed similarities to a_mMIL-125-NH_2, Fig. S14 (ESI†), though further analysis is needed to confirm specific structures. Comparisons were also made to TiO_2, both rutile and anatase (Fig. S14d and e, ESI†), which showed limited correlation with the peaks in a_mMIL-125-NH_2, past what is defined by Ti–O bond length. This does not, however, rule out the formation of small clusters of Ti–O, separate to that held within the SBU.

Fourier-transform infrared (FTIR) spectroscopy confirmed changes in linker-binding mode upon amorphisation (Fig. S18 and Table S7, ESI†). Significant broadening of carbonyl vibration peaks, both symmetric and asymmetric, suggests a mix of divalent, monovalent, and uncoordinated linkers, indicating distortion in the linker binding environments.[19] Increased peak intensity at 1689 cm^{-1} and 1567 cm^{-1} were characteristic of the presence of uncoordinated and monocoordinated linker, respectively.[20,21] These observations suggest that the amorphisation involves M–L bond breakage and the formation of a high concentration of linker-based defects. Broadening in the 400–800 cm^{-1} range indicates changes in the O–Ti–O bonds, consistent with SBU collapse or rearrangement.[12]

Thermogravimetric analysis (TGA) was used to investigate missing-linker defects (Fig. S19, ESI†).[22] TGA of two samples of a_mMIL-125-NH_2, one with prolonged exposure to air, showed increased weight loss from solvent evaporation, suggesting rapid coordination of atmospheric water capping missing-linker defects.[20] Few compositional changes were detected (Tables S8, S9 and Fig. S19, ESI†), likely due to missing linkers being trapped in the pores or through mono-coordination. Washing a_mMIL-125-NH_2 removed the trapped linkers, with an SBU : linker ratio of 1 : 2.97 from 1 : 4.99 being detected, confirming the presence of a high concentration of missing linker defects, (Fig. S20, ESI†). CHN confirmed no large quantity of TiO_2 had been produced.

These missing-linker defects could be valuable for *a*MOF applications. MIL-125-NH_2 has shown promising photocatalytic activity due to linker-to-metal charge transfer (LMCT) under visible light exposure.[23] The localisation of the LUMO and HOMO, on the metal cluster and organic linker, respectively, inhibits fast electron–hole recombination, enhancing photocatalytic efficiency.[23] Since amorphisation alters M–L bonds and increases the number of accessible Ti active sites, it likely affects photocatalytic performance.[23,24] This is supported by the notable shift in colour observed upon amorphisation, indicative of a change in band gap energy, Fig. S21 (ESI†). This could present a way of tuning the band gap for specific applications through the controlled introduction of these defects. While band gap engineering has focused on crystal facet growth and defect control, the impact of combined defects and disorder on photocatalysis remains underexplored.[23,24]

Reflectance UV-Vis (RUV-Vis) spectroscopy, employed to investigate this colour change, showed a key absorbance at ~380 nm, attributed to the LMCT band (Fig. 4a and Fig. S22, ESI†).[23,24] A Kubelka–Munk transformation of the RUV-Vis data extracted a band gap value for the crystalline material consistent with the literature (Fig. 4b).[23,24] Amorphisation caused a red-shift in the band gap from 2.80 eV to 2.72 eV, aligning with the observed colour change and absorbance shift.

The photocatalytic activity of the crystalline and amorphous materials was tested *via* the oxidative coupling of amines to imines (Scheme S1, ESI†). Although the amorphous sample showed higher absorbance at the irradiated wavelengths (Fig. S24, ESI†), the photocatalytic activity was slightly lower (Table S10, ESI†). This suggested that factors beyond band gap energy, that are affected by the amorphisation process, *e.g.* particle size, morphology, structural arrangements and/or porosity, also influence the photocatalytic performance of a_mMIL-125-NH_2.[3,13]

N_2 and CO_2 adsorption isotherms (Fig. S25, ESI†) showed a significant drop in sorption capacity for the amorphous material. The BET surface area of MIL-125-NH_2 decreased from 785 $m^2\ g^{-1}$ to 51 $m^2\ g^{-1}$ after amorphisation. As photocatalytic reactions rely on a large accessible surface area to reach defects sites, balancing defect concentration and porosity is crucial for optimal activity. Whilst a decrease in overall photocatalytic activity is observed, relative to the substantial reduction in surface area, amorphisation was found to enhance the intrinsic photocatalytic activity of the material. Solvent-assisted stabilisation could help retain some of the original porosity while introducing defects.[16]

In conclusion, ball-milling amorphisation in MIL-125-NH_2 occurs *via* missing-linker defects, M–L bond breakage, and

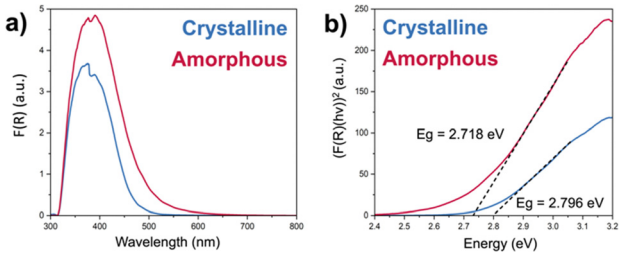

Fig. 4 (a) UV-Vis diffuse reflectance spectra of MIL-125-NH_2 (blue) and a_mMIL-125-NH_2 (red). Due to the absorbance of glass, features below 300 nm have been subtracted as background. The feature observed at ~400 nm was attributed to a change between detectors, required to measure across the whole wavelength range. (b) Tauc plot.

partial SBU distortion. Further analysis of short-range order is needed to identify the dominant factor. These structural changes affect the band gap, which, with other parameters, could be tuned to influence photocatalytic properties. The results highlight ball-milling as a promising method for defect engineering in MOFs.

C. C. B. and T. D. B. designed the project. E. V. S. wrote the original manuscript with inputs from all authors. E. V. S. preprepared and characterized the materials by PXRD, SEM, TGA and FTIR. TEM data was collected by J. E. M. L. and P. A. M., with T. L. performing the analysis. Total scattering data were collected by C. C. B., G. P. R., D. A. K. and A. M. C., and analysed by E. V. S., with inputs from C. C. B. and D. A. K. S. G. collected the XPS data. C. Y., V. M., K. U. and B. K. collected the *in situ* mechanochemical PXRD, with analysis by G. I. L. B. T. and L. N. M. collected the N_2 and CO_2 isotherms. B. S., S. C., A. F. and J. A. performed the photocatalytic tests. UV-Vis data were collected by J. K. G. K., and analysed by E. V. S., with supervision from R. C. E.

Authors thank the Leverhulme Trust (RPG-2020-005) (T. D. B., C. C. B., A. M. C.), the Royal Society for both a University Research Fellowship (URF\R\211013) (T. D. B.) and a research grant (RGS\R2\212221) (T. D. B.), UKRI and Diamond light source (STU0366) (G.P.R.), the EPSRC Cambridge NanoDTC (EP/S022953/1) (T. L.), St Edmunds College (C. Y.), the Croatian Science Foundation (IP-2020-02-4702) (V. M., I. B., B. K. and K. U.), the Spanish MICINN (PID2021-122299NB-100) (B. S., S. C., J. A. and A. F), the University of Liverpool (L. N. M., B. T.), and the ERC European Union's Horizon 2020 research and innovation programme (Grant Agreement No. 818762) (R. C. E., J. K. G. K.). We acknowledge DESY (Hamburg, Germany), a member of the Helmholtz Association HGF, for the provision of experimental facilities. Parts of this research were carried out at PETRA III and we would like to thank M. Etter for assistance in using beamline P02.1. Beamtime was allocated for proposals I-20221330 EC and I-20230031 EC.

Data availability

The data supporting this article have been included as part of the ESI,† for scanning electron microscopy and transmission electron microscopy characterisation and photocatalysis tests. Data for this article, including DSC, PDF and X-ray analysis, FTIR, gas sorption isotherms, TGA, XPS and UV-vis spectroscopy are available at Open Science Framework at DOI **https://doi.org/10.17605/OSF.IO/3UQY**T.

Conflicts of interest

There are no conflicts to declare.

References

1 T. D. Bennett and A. K. Cheetham, *Acc. Chem. Res.*, 2014, **47**, 1555–1562.
2 J. Fonseca, T. Gong, L. Jiao and H.-L. Jiang, *J. Mater. Chem. A*, 2021, **9**, 10562–10611.
3 E. V. Shaw, A. M. Chester, G. P. Robertson, C. Castillo-Blas and T. D. Bennett, *Chem. Sci.*, 2024, **15**, 10689–10712.
4 J. Fonseca and S. Choi, *Catal. Sci. Technol.*, 2020, **10**, 8265–8282.
5 H. Wang, Q. Yang, N. Zheng, X. Zhai, T. Xu, Z. Sun, L. Wu and M. Zhou, *Nano Res.*, 2023, **16**, 4107–4118.
6 T. D. Bennett, P. J. Saines, D. A. Keen, J.-C. Tan and A. K. Cheetham, *Chem. – Eur. J.*, 2013, **19**, 7049–7055.
7 Y. Shan, G. Zhang, Y. Shi and H. Pang, *Cell Rep. Phys. Sci.*, 2023, **4**, 101301.
8 A. M. Belenguer, A. A. L. Michalchuk, G. I. Lampronti and J. K. M. Sanders, *Beilstein J. Org. Chem.*, 2019, **15**, 1226–1235.
9 T. Panda, S. Horike, K. Hagi, N. Ogiwara, K. Kadota, T. Itakura, M. Tsujimoto and S. Kitagawa, *Angew. Chem., Int. Ed.*, 2017, **56**, 2413–2417.
10 T. D. Bennett, T. K. Todorova, E. F. Baxter, D. G. Reid, C. Gervais, B. Bueken, B. Van de Voorde, D. De Vos, D. A. Keen and C. Mellot-Draznieks, *Phys. Chem. Chem. Phys.*, 2016, **18**, 2192–2201.
11 B. Kim, Y.-R. Lee, H.-Y. Kim and W.-S. Ahn, *Polyhedron*, 2018, **154**, 343–349.
12 M. Dan-Hardi, C. Serre, T. Frot, L. Rozes, G. Maurin, C. Sanchez and G. Férey, *J. Am. Chem. Soc.*, 2009, **131**, 10857–10859.
13 C. Zlotea, D. Phanon, M. Mazaj, D. Heurtaux, V. Guillerm, C. Serre, P. Horcajada, T. Devic, E. Magnier, F. Cuevas, G. Férey, P. L. Llewellyn and M. Latroche, *Dalton Trans.*, 2011, **40**, 4879–4881.
14 A. F. Sapnik, C. Sun, J. E. M. Laulainen, D. N. Johnstone, R. Brydson, T. Johnson, P. A. Midgley, T. D. Bennett and S. M. Collins, *Commun. Chem.*, 2023, **6**, 92.
15 C. L. Farrow, P. Juhas, J. W. Liu, D. Bryndin, E. S. Božin, J. Bloch, T. Proffen and S. J. L. Billinge, *J. Condens. Matter Phys.*, 2007, **19**, 335219.
16 A. F. Sapnik, D. N. Johnstone, S. M. Collins, G. Divitini, A. M. Bumstead, C. W. Ashling, P. A. Chater, D. S. Keeble, T. Johnson, D. A. Keen and T. D. Bennett, *Dalton Trans.*, 2021, **50**, 5011–5022.
17 T. D. Bennett, S. Cao, J. C. Tan, D. A. Keen, E. G. Bithell, P. J. Beldon, T. Friscic and A. K. Cheetham, *J. Am. Chem. Soc.*, 2011, **133**, 14546–14549.
18 A. F. Sapnik, I. Bechis, A. M. Bumstead, T. Johnson, P. A. Chater, D. A. Keen, K. E. Jelfs and T. D. Bennett, *Nat. Commun.*, 2022, **13**, 2173.
19 N. J. Castellanos, Z. Martinez Rojas, H. A. Camargo, S. Biswas and G. Granados-Oliveros, *Transition Met. Chem.*, 2019, **44**, 77–87.
20 K. Tan, H. Pandey, H. Wang, E. Velasco, K.-Y. Wang, H.-C. Zhou, J. Li and T. Thonhauser, *J. Am. Chem. Soc.*, 2021, **143**, 6328–6332.
21 Z. Su, Y.-R. Miao, G. Zhang, J. T. Miller and K. S. Suslick, *Chem. Sci.*, 2017, **8**, 8004–8011.
22 G. C. Shearer, S. Forselv, S. Chavan, S. Bordiga, K. Mathisen, M. Bjørgen, S. Svelle and K. P. Lillerud, *Top. Catal.*, 2013, **56**, 770–782.
23 V. Kavun, E. Uslamin, B. van der Linden, S. Canossa, A. Goryachev, E. E. Bos, J. Garcia Santaclara, G. Smolentsev, E. Repo and M. A. van der Veen, *ACS Appl. Mater. Interfaces*, 2023, **15**, 54590–54601.
24 L. Pukdeejorhor, S. Wannapaiboon, J. Berger, K. Rodewald, S. Thongratkaew, S. Impeng, J. Warnan, S. Bureekaew and R. A. Fischer, *J. Mater. Chem. A*, 2023, **11**, 9143–9151.

